

www.acsanm.org Article

Development of Broadband PbS Quantum Dot/Graphene Photodetector Arrays with High-Speed Readout Circuits for Flexible Imagers

Andrew Shultz,*,[⊥] Bo Liu,*,[⊥] Maogang Gong, Mohammed Alamri, Michael Walsh, Russell C. Schmitz, and Judy Z. Wu*



Cite This: ACS Appl. Nano Mater. 2022, 5, 16896-16905



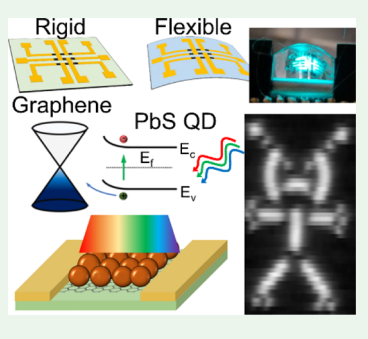
ACCESS I

III Metrics & More

Article Recommendations

Supporting Information

ABSTRACT: Colloidal quantum dot (QD)/graphene nanohybrid heterostructures provide a promising scheme for quantum sensors as they take advantage of the strong quantum confinement in QDs with enhanced light—matter interaction, spectral tunability, suppressed phonon scattering, and extraordinary charge mobility in graphene at room temperature. Herein, we report development of a flexible, nine-channel PbS QD/graphene nanohybrid imaging array on polyethylene terephthalate using a facile process for device fabrication, signal acquisition, and processing. The PbS QD/graphene imaging array exhibited high and uniform photoresponse. At a 1.0 V bias, the highest responsivity was $9.56 \times 10^3 - 3.24 \times 10^3$ A/W for 400 - 1000 nm incident light [ultraviolet—visible—near-infrared (UV—vis—NIR)] with a power of 900 pW. In addition, the array has a consistent spectral response with bending down to a radius of curvature of a few millimeters. The demonstration of imaging at broadband wavelengths in the UV—vis—



NIR range indicates that QD/graphene nanohybrids provide a viable approach for flexible photodetectors and imagers.

KEYWORDS: quantum dots, graphene, nanohybrid photodetector, flexible, broadband imaging array

1. INTRODUCTION

Colloidal quantum dot (QD)/graphene nanohybrid heterostructures have recently emerged as a promising scheme for photodetectors. The nanohybrid takes advantage of the strong quantum confinement in QDs that leads to enhanced lightmatter interaction, spectral tunability, as well as suppressed phonon scattering, 2-4 and in graphene, a 2D atomic sheet of carbon atoms arranged in a hexagonal lattice, quantum confinement enables extraordinary charge carrier mobility at room temperature. 5-9 In the QD/graphene nanohybrid photodetectors, the optoelectronic process includes three steps: light absorption by QDs, dissociation of photo-generated excitons in QDs by the built-in electric field at the QD/ graphene interface, and charge transfer across the interface. The last step of charge transfer is driven by the built-in electric field at the QD/graphene interface, with one type of charge carrier transferred to graphene while the other oppositely charged carrier is trapped in the QDs. The exciton lifetime is much enhanced in QDs as compared to that in bulk semiconductors due to the quantum confinement. 10 The trapped charge in QDs will generate a so-called photogating effect on graphene, which alters the electrical conductivity of the graphene channel as the photoresponse. The QD/ graphene nanohybrids could have a large photoconductive gain that is proportional to the ratio of the exciton lifetime in QDs and charge carrier transit time (inversely proportional to charge carrier mobility in graphene) in the graphene channel.

Consequently, this high gain yields high photoresponse and high detectivity $(D^*)^1$. The absorption spectrum of PbS QDs covers from ultraviolet and visible to near-infrared (UV-vis-NIR). This means that PbS QD/graphene nanohybrid photodetectors have the capability for broadband photodetection. D* values of 1013 and 1012 Jones have been reported recently under 532 and 1550 nm incident wavelengths, respectively, on PbS QD/graphene nanohybrid photodetectors. QDs of many other materials have also been explored in QD/graphene nanohybrid photodetectors. For example, CsPbBr_{3-x}I_x perovskite QD/graphene photodetector has achieved a D^* of 10^{16} Jones in the detection range of 400-700 nm, 11 and ZnO QD/graphene vdW heterostructure photodetectors with a D^* of 10^{13} Jones were also reported for UV detection. 12 Graphene-based devices incorporating nanorods of PbS have been recently demonstrated to have a high D^* of 10^9 Jones at a wavelength of 2.7 μ W. ¹³ Recent advances in detectors incorporating graphene without QDs, such as Te-hyperdoped silicon, have shown an impressive D* of 10^9 Jones at a wavelength of 1.55 μ m. Use of a silicon

Received: August 30, 2022 Accepted: October 24, 2022 Published: November 3, 2022





grating has been recently shown to greatly enhance the photogating in monolayer graphene, achieving a very high D^* of 10^{12} Jones at a wavelength of 1.55 μ m. ¹⁵

Developing photodetectors into an array is critical to practical applications for imaging. A PbS QD/graphene nanohybrid photodetector array could achieve broadband imaging with high sensitivity at room temperature. Koppens et al. reported a broadband image sensor by integrating a PbS QD/graphene nanohybrid focal plane array (FPA) with complementary metal-oxide-semiconductor (CMOS) readout-integrated circuits (ROICs) for broadband imaging up to 2000 nm. ¹⁶ One limitation of the CMOS is that it is difficult to be achieved on a curved surface which would reduce total optics and remove the need for aspherical elements, therefore significantly reducing the cost for imaging.¹⁷ Owing to the flexibility and transferability of QD/graphene nanohybrid photodetectors, a curved imager could be realized by fabricating the QD/graphene nanohybrid array on a flexible substrate. It should be noted that intensive research has been carried out recently on flexible image sensors and exciting progress has been obtained. $^{18-24}$ However, flexible FPAs based on the QD/graphene heterostructures with compatible ROIC remain a challenge, despite the advantages of spectral selectivity through implementation of QDs of different optical cutoffs that is further tunable by the QD size, the ultrahigh gain stemming from the strong quantum confinement from both QD and graphene (hence superior carrier mobility), and the inherent flexibility and low cost. In fact, the flexible QD/ graphene nanohybrid sensor is suitable for wearable devices, which can be integrated with technologies such as wireless readout and battery-free circuitry.²⁵ Designing a PbS QD/ graphene nanohybrid array with a compatible ROIC will be imperative toward flexible image sensor applications.

In this work, a 3 × 3-pixel PbS QD/graphene nanohybrid photodetector array (9-channel sensor array) was fabricated on a flexible substrate of acetone-resistant polyethylene terephthalate (PET) as a proof-of-concept. It should be noted that PbS QDs have been shown to have a broadband absorption in UV-vis-NIR or even to short-wave infrared spectra by increasing the QD dimension. We show that controlling the QD/graphene interface is critical to achieve high performance and pixel uniformity. For broadband imaging in the UV-vis-NIR spectrum, a low-cost Arduino ROIC was designed and employed, demonstrating promising applications of flexible PbS QD/graphene FPAs.

2. EXPERIMENTAL SECTION

2.1. Fabrication of QD/Graphene Nanohybrid Imaging Sensor Arrays on PET and Si Substrates. Preparation of the nine-channel PbS QD/graphene nanohybrid imaging sensor arrays started with cleaning the PET and SiO2/Si substrates by rinsing with acetone, isopropanol, and reverse osmosis water, respectively, repeated three times. The SiO₂/Si substrate was adopted for optimization of the sensor fabrication protocol with respect to responsivity and response speed in UV-vis-NIR spectra. The substrate cleaning was followed by deposition of Nb (40 nm)/Pd (10 nm) electrodes on the substrates via DC sputtering at 330 W/45 W in high vacuum (5 \times 10⁻⁷ Torr) with an Ar gas operating pressure of 14 mTorr/30 mTorr. Use of a custom-made shadow mask during sputtering created the electrode pattern designed for the nine-channel PbS QD/graphene nanohybrid sensor array. Single-layer graphene was grown on polycrystalline copper foil of 50 µm thickness (Sigma-Aldrich) using chemical vapor deposition at 1050 °C in mixed H₂/27 CH₄ gases. Details can be found in our previous reports.²⁴ Graphene was then wet transferred on top of the substrate with

prefabricated electrodes following the method reported earlier. ^{28,29} Photolithography was carried out to define the graphene channels, followed with reactive ion etching (RIE) of unwanted graphene in oxygen plasma in an RF RIE system (Torr International).

PbS QDs were synthesized in an Ar environment using our previously reported Schlenk line system method.³⁰ A micropipette was used to transfer ~10 μL of PbS QD suspended in 10 mL of chloroform and deposited onto the substrate using a SonoPlot Microplotter Proto ink-jet printer. Printing helps to maintain a uniform thickness of PbS QDs over all nine devices in a sample as well as keeping the electrodes clean for wiring after deposition. Each printing scan deposits a layer of PbS QDs about 10 nm thick.³⁰ Due to different wettabilities of the PET substrates, the thickness of the PbS QDs on PET is considerably thinner than that on the Si substrate. In this work, 12 printing scans were used to obtain a PbS QD layer thickness of about 100 nm on Si substrates. Since the photoresponsivity and response speed both are determined by the efficiency of charge transfer across the QD/graphene interface, 10,12 controlling the interface is a critical step for high-performance QD/ graphene photodetectors. For PbS QD/graphene photodetectors, a ligand-exchange process was developed to establish such a charge transfer across the QD/graphene interface. Specifically, conductive short-chain 3-mercaptopropionic acid (MPA) was used to replace the insulating long-chain ligands of oleylamine (OLA) and oleic acid (OA) attached on the PbS QD surface from the synthesis solution.³¹ It should be noted that the MPA ligands have been shown to passivate the QD surface against ambient degradation. 20,29 Experimentally, multiple MPA ligand exchanges were applied to obtain optimal QD/ graphene interface. For each MPA ligand exchange, the substrate was gently dipped in MPA for 1 min to exchange the OLA and OA ligands attached on the PbS QD surface. The ink-jet printing (four scans) and ligand exchange were repeated three times to achieve a film of PbS QDs about 100 nm thick on Si substrates. The ligand-exchange process helps with surface passivation, QD stability, and charge transfer. Last, the nine-sample array was wired to a chip carrier with platinum wire (50 μ m in diameter) using colloidal silver paint on the substrate side and solder on the chip carrier side.

2.2. Sample Characterization. The optical absorption spectrum of PbS QDs was collected using a UV-3600 Shimadzu spectrometer. The crystal structure and morphology of the PbS QDs were characterized using field-emission transmission electron microscopy (FETEM) on a FEI Tecnai F20XT system with an accelerating voltage of 200 kV. Raman spectra of graphene were obtained with a WiTec Alpha300 confocal micro-Raman system equipped with a piezoelectric sample stage using a 488 nm excitation laser. PbS QD film thickness was measured with a KLA Tencor P-16 profiler.

2.3. Arduino-Based ROIC. Simultaneous device characterization for all nine pixels is possible using an Arduino-based ROIC. A custom Arduino shield was designed and employed to increase the Arduino's functionality. Selecting individual devices for testing is achieved by use of two multiplexers. Readout is accomplished using a voltage divider consisting of a programmable resistor (100-5000 Ω), to control sensitivity, and the device under test. The voltage drop across the variable resistor (the signal) is then partially nulled by a differential amplifier and a programmable digital-to-analog converter. The partially nulled signal is amplified by a factor of 2 by the differential amplifier and can be further amplified by a programmable gain amplifier up to a total gain of 64. Last, the amplified signal (voltage drop across the reference resistor) is read by an external analog-to-digital converter (0-3.3 V with 12 bit precision) and the raw binary data sent via serial port to a computer. Crosstalk between devices sharing an electrode is prevented by applying a voltage equal to the voltage drop across the device under test, via an op-amp voltage follower, to the other electrode of the device not being measured. This control of the Arduino and all its programmable elements is achieved by custom software written in LabView. The process for reading out the array is illustrated in Figure S3. The Arduino samples the whole array 130 times every second, fast enough to allow simultaneous data acquisition for all nine devices. The data being collected by the Arduino is the voltage across the variable resistor with

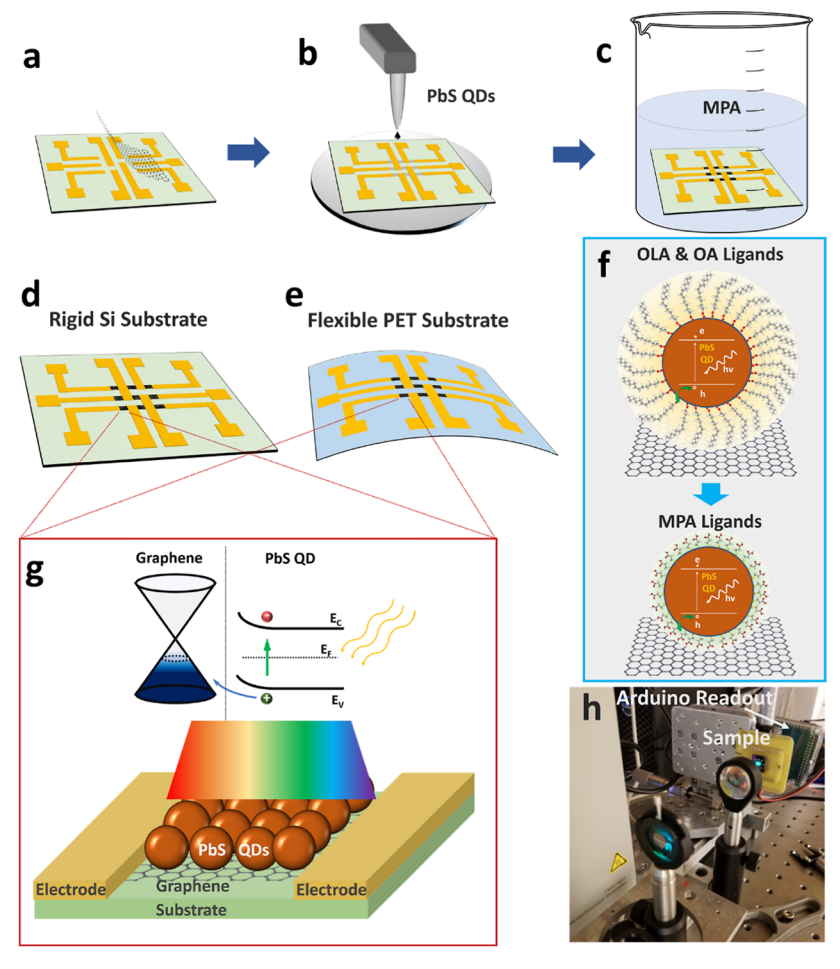


Figure 1. (a–c) Device fabrication process of the nine-channel PbS QD/graphene sensor array. (a) Graphene transfer on substrates with prefabricated Pd/Nb electrodes; (b) PbS QD coating on graphene channels; and (c) MPA ligand exchange. (d,e) are schematic drawing of the nine-channel PbS QD/graphene sensor array fabricated on rigid Si and flexible PET substrates, respectively. (f) Schematic description of replacing long-chain, insulating OLA and OA ligands that encapsulate PbS QDs with short-chain, conductive MPA ligands in order to facilitate charge transfer from QDs to graphene. (g) Schematic illustration of the structure of a pixel in the nine-channel PbS QDs/graphene sensor array and the built-in electric field at the PbS QD/graphene interface. (h) Optical setup of the transmission imaging on the nine-channel PbS QD/graphene photodetector array using Arduino-based readout.

different devices under test. These voltages are then used to calculate measures of performance, such as responsivity.

2.4. Optoelectronic Characterization on PbS QD/Graphene Sensor Arrays. The light source used for optoelectronic characterization and imaging was a Newport Oriel Apex Monochromator illuminator which fed into the accompanying Newport Oriel Cornerstone 130 1/8m Monochromator for wavelength selection in the spectrum of UV-vis-NIR. The light density was varied using neutral density filters inserted into the light path after the monochromator. For imaging characterization, two approaches were adopted in this work. One was live imaging using all pixels of the ninechannel PbS QD/graphene FPAs. Considering the limited number of pixels and hence limited spatial resolution of the nine-channel PbS QD/graphene FPAs, a scanning stage was used for imaging using a single pixel on the FPA to allow images to be taken under different experimental conditions. Converging lenses were employed to focus the light onto the image location. The position of the object to be imaged was varied by an XY stage moved by two linear actuators and controlled by the same LabView program as the Arduino. Data acquisition during image scanning was continuous with a sampling rate of 1200 Hz by the ROIC for one pixel of an FPA with up to $16 \times$ 16 pixels. With the best response speed of ~100 to 200 Hz observed on PbS QD/graphene photodetectors, the ROIC frame rate is adequate. The linear actuators moved at a maximum speed of 0.2 mm/s and with a horizontal scan length of 2 mm, leading to a step

size of 17 μ m for the horizontal direction. A total of 80 horizontal scans were collected, moving upward in the vertical direction after each horizontal scan to form an image. Scan length in the vertical direction was 4 mm that makes the step size 50 μ m in the vertical direction and a total scan time of 13 min. It should be noted that scan time is limited by the speed of the linear actuators. The center pixel was used for the image scans for both Si and PET arrays. The monochromator was controlled via plain text commands sent over a serial connection (USB). This allows tying together wavelength selection, shutter control (light on/off), image movement, and the Arduino ROIC into a single LabView computer program for a flexible as well as inexpensive characterization/imaging system.

2.5. Bending Mechanism for Nine-Channel PbS QD/Graphene Sensor Array on PET Substrate. A sample bending vise was made to test the performance of the PbS QD/graphene/PET sensor array at different radii of curvature. The vise was mounted on a 30-pin chip carrier with electrical connection by a platinum wire of 50 μ m diameter. The screw, which opens/closes the vise, was rotated incrementally, and for each bent state, the spectral response was measured. Bending was increased until the sensor array's response started to deteriorate.

2.6. Statistical Analysis. Responsivity, detectivity, rise time, and fall time were found from the average of three light on/light off cycles in the dynamic photoresponse measurement. The standard deviation of these three cycles defines the error bars on all relevant plots and

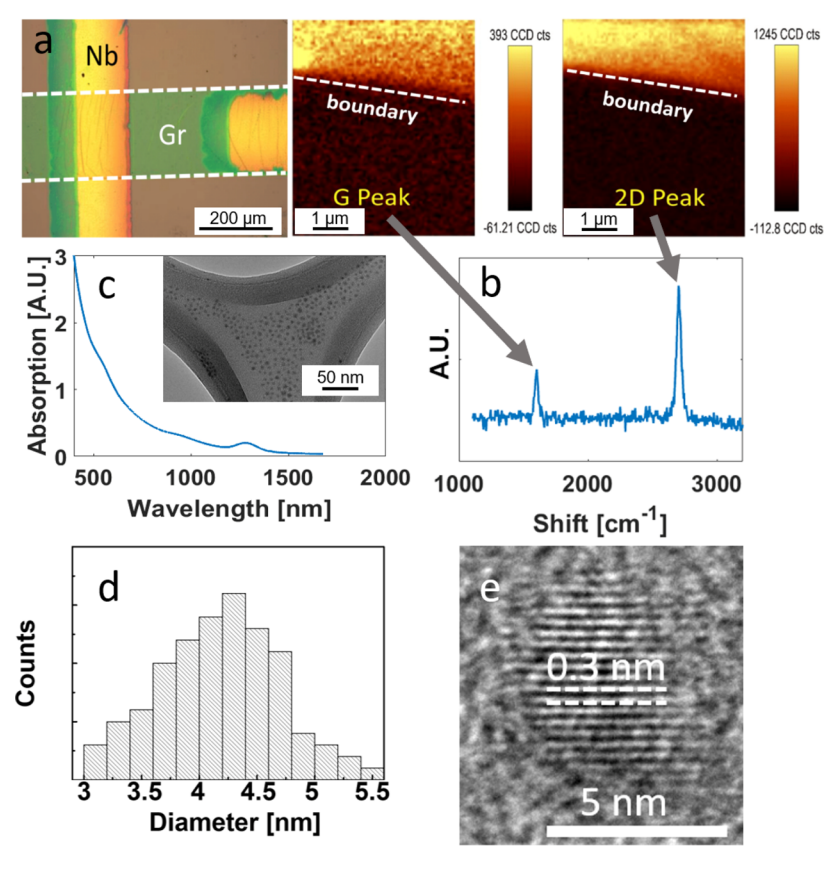


Figure 2. (a) Optical image of a graphene, or "Gr", channel on a nine-channel PbS QD/graphene sensor array just prior to QD deposition. (b) Raman maps of the G-peak (top-left) and 2D-peak (top-right) at the boundary between graphene/Si and Si as well as a Raman spectrum for a randomly chosen spot on the graphene. The I_{2D}/I_G is > 2, which is expected for monolayer graphene. (c) Absorption spectrum of the PbS QDs showing an absorption peak near 1200 nm. The inset shows a TEM image of the PbS QDs, indicating the size and uniformity of the PbS QDs. (d) Distribution of the PbS QD diameter size. (e) High-resolution TEM image of a PbS QD. The fringe spacing is about 0.3 nm, which corresponds to the (200) lattice planes of PbS ($d_{200} = 0.297$ nm, JCPDS card, reference code 03-065-0692).

quantities. The data was used as taken, and no preprocessing was needed.

3. RESULTS AND DISCUSSION

Figure 1 illustrates the process developed in this work for fabrication of nine-channel PbS QD/graphene nanohybrid sensor arrays on PET and Si substrates. Specifically, Figure 1a shows the layout of the electrodes designed for the nine graphene channels. The selection of Pd as the metal contact to graphene is based on the consideration of the match of the work functions between the two materials, the stability of Pd in air, and chemicals adopted for wet transfer of graphene on top of the electrodes. Figure 1b exhibits the nine graphene channels fabricated using photolithography. The dimension of the channel is 220 μ m (L) \times 400 μ m (W). PbS QDs were deposited on the graphene channel, followed by MPA ligand exchange, as shown in Figure 1c schematically. The obtained nine-channel PbS QD/graphene nanohybrid sensor arrays on Si (rigid) and PET (flexible) substrates are illustrated in Figure 1d,e, respectively. It should be noted that the ligand exchange plays a critical role in achieving high photoresponse and high response speed in PbS QD/graphene photodetectors.³¹ As shown in the top panel of Figure 1f, the as-synthesized PbS QD is typically passivated with long-chain ligands, primarily OA and OLA, in the synthesis solvent. Since these ligands are insulating, they form a charge-transfer blocking layer at the PbS QD/graphene interface, which means no photoresponse may

be achieved. The MPA ligand exchange replaces the insulating OA and OLA ligands with short-chain, highly conductive MPA ligands. Charge transfer from PbS QD to graphene is facilitated by the MPA ligands. As shown in Figure 1g, this charge transfer is driven by the built-in electric field at the PbS QD/graphene interface due to the band-edge alignment. MPA ligands can also passivate the surface states on the QD surface reducing their charge-trapping effect, thus enhancing efficient charge transfer across the interface, which is the key to high responsivity and response speed. Figure 1h shows a picture of the optical setup and Arduino ROIC used for characterization of the obtained nine-channel PbS QD/graphene nanohybrid sensor arrays.

Figure 2a shows an optical image of one pixel on a nine-channel PbS QD/graphene sensor array before QD deposition. To examine the quality of the graphene, Raman spectra were taken at three spots randomly selected on the graphene channel and the results are shown in Figure 2b. The two characteristic graphene peaks correspond to G (at 1585 cm $^{-1}$) and 2D bands (at 2668 cm $^{-1}$). The G band is associated with the primary in-plane vibrational mode, and the 2D band is the second order of the D band (at 1356 cm $^{-1}$) that corresponds to the A1g breathing mode of the hexagonal rings. The ratio of the 2D and G band intensities ($\rm I_{2D}/\rm I_{G}$, with each intensity measured from the noise background to the top of the peak) is $\sim\!\!2.8$, and the negligible intensity of the D peak indicates that the graphene is a single layer with a low concentration of

defects. Raman 2D and G peak maps (insets of Figure 2b) were taken near the edge of the graphene channel, in which a clear graphene/SiO₂ boundary could be observed. Figure 2c shows the optical absorption spectrum of the PbS QDs with an absorption peak of 1258 nm. This means that the PbS QD/ graphene nanohybrids would be effective for photodetection in the broadband of UV-vis-NIR. The inset displays a fieldemission transmission electron microscopy (FETEM) image of PbS QDs with an approximately spherical morphology. High crystallinity of the PbS QDs has been confirmed using highresolution TEM (HRTEM) as shown in a zoom-in view of a PbS QD in Figure 2e. The average diameter of 4.18 nm has been extracted from the histogram of the PbS QD size shown in Figure 2d. It should be noted that changing the dimension of the PbS QD would allow tuning of the absorption designed for photodetection in different spectra, which is a unique advantage of the QD/graphene nanohybrid photodetectors.

The completed array has a PbS QD film thickness of 250-350 nm. Figure 3a compares the dynamic photoresponse of a

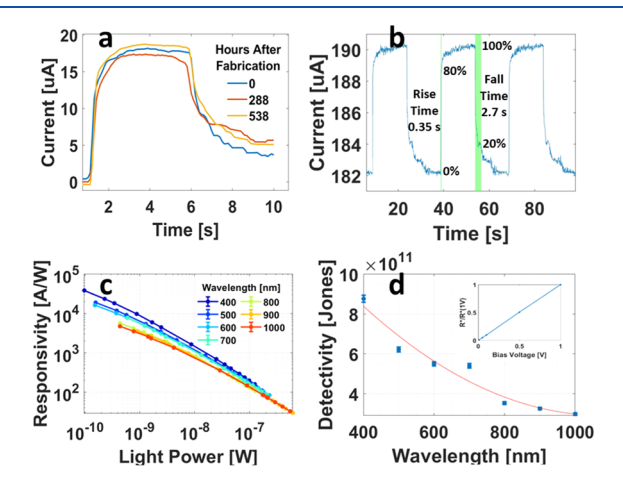


Figure 3. (a) Dynamic photoresponse of a selected pixel on a ninechannel PbS QD/graphene sensor array on the Si substrate at a few selected times after fabrication. The incident light has a power of 230 nW and a wavelength of 500 nm. The bias voltage across the pixel was 1.0 V. (b) Three light on/off cycles showing the reproducibility as well as the rise and fall times as defined. (c) Photoresponsivity of the same nine-channel PbS QD/graphene sensor array vs incident light power for a few selected wavelengths in the range of 400-1000 nm. The bias voltage across the pixel was 1.0 V. (d) Detectivity of the same nine-channel PbS QD/graphene sensor array vs wavelength for an incident light power of 900 pW and a bias voltage of 1.0 V. The inset shows normalized responsivity of the same nine-channel PbS QD/graphene sensor array vs bias voltage for an incident light power of 900 pW and a wavelength of 500 nm. The data has been normalized at the 1 V responsivity of 6783 A/W.

single pixel of a nine-channel PbS QD/graphene sensor array on the Si substrate measured immediately after the array fabrication was completed (blue) and at 288 h and 538 h afterward. The three curves coincide approximately on each other, indicating the PbS QD/graphene sensors have an excellent stability after the fabrication is completed. The rise (0-80%) and fall (100-20%) time constants are estimated to be 0.35 s \pm 0.08 s and 2.7 s \pm 0.5 s respectively, as seen in Figure 3b, for a chopper frequency of 0.033 Hz (15 s light on and 15 s light off). At a chopper frequency of 55 Hz, the rise and fall times drop to 2.3 ms \pm 0.5 ms and 5.6 ms \pm 1.0 ms, respectively, as seen in Figure S2. It should be pointed out that the asymmetric dynamic response and the tails in both rise and fall are indicative of residual charge traps on the PbS QD surface and/or PbS QD/graphene interface. 10 The charge traps are often associated to the QD surface states and the QD/ graphene interface contaminated with various unintended molecules or chemical agents adsorbed to the interface.³³ Much improved response speed and symmetry in dynamic response through passivation of the QD surface states and improvement of the QD/graphene interface have been achieved. 12,34 This suggests that further improvement of the response speed of the PbS QD/graphene sensors is possible through surface and interface engineering.

Photoresponsivity (R^*) is an import metric to characterize a photodetector, which is defined as the ratio of photocurrent to the power of the light incident on the device

$$R^* = \frac{I_L - I_D}{P_0}$$

Figure 3c exhibits the calculated R^* as a function of the power of incident light at wavelengths of 400-1000 nm in 100 nm increments. All curves show monotonically increasing R* values with decreasing light power, which is consistent with the literature due to the more efficient light detection at low power with reduced nonradiative recombination. [6, 14] With decreasing wavelengths, the R^* value increases monotonically, which is ascribed to the higher kinetic energy of photo-excited charge carriers (and hence lower charge recombination) by shorterwavelength photons. Nevertheless, high R* values have been observed in the entire UV-vis-NIR spectrum, as shown in Figure 3c. At 400 nm wavelength (UV), the R^* value is up to $9.56 \times 10^3 \text{ A/W} \pm 0.20 \times 10^3 \text{ A/W}$. At 500 nm, it decreases slightly to 6.78×10^3 A/W $\pm 0.15 \times 10^3$ A/W, while at 1000 nm, a high R* value up to $3.24 \times 10^{3} \text{ A/W} \pm 0.07 \times 10^{3} \text{ A/W}$ can be obtained for an incident light power of 900 pW. A chopper speed of 0.033 Hz was used to measure these R* values. If a chopper speed of 55 Hz is used, the R* values would decrease by a factor of ~40. It should be noted that the responsivity of the R* remains approximately linear across the dynamic range of 10⁻⁷ to 10⁻⁹ W in broadband of 400–1000 nm in Figure 3c, which is important in practical applications. A moderate deviation from the linear trend occurs at lower optical power, which may be further improved through optimization of the device design. The linear trend of responsivity at higher optical powers holds for the whole array, as shown in Figure S5, for an incident wavelength of 550

The specific detectivity (D^*) is a key figure of merit for photodetectors and can be calculated based on the equation $D^* = (A \times \Delta f)^{1/2}/\text{NEP}, ^{20,35,36}$ where A is the detector area in cm², and NEP is the noise equivalent power with the units of W/Hz^{1/2}, which is defined as the minimum optical power required to obtain a unity signal-to-noise ratio. NEP can be calculated from equation NEP = I_n/R^* , where I_n is the mean square noise current, which can be obtained from the spectra density of the noise power, and R* is the photoresponsivity. The current density noise spectra of the nine-channel PbS QD/graphene sensor array show that I_n monotonically decreases with increasing frequency, which is enabled by fitting $I_n \propto 1/f$ in the low-frequency range up to kilohertz (Figure S1), indicating the 1/f noise dominates the noise current behavior at low frequencies. The working bandwidth (Δf) is 1 Hz, and the value of I_n is found from a fit to the noise

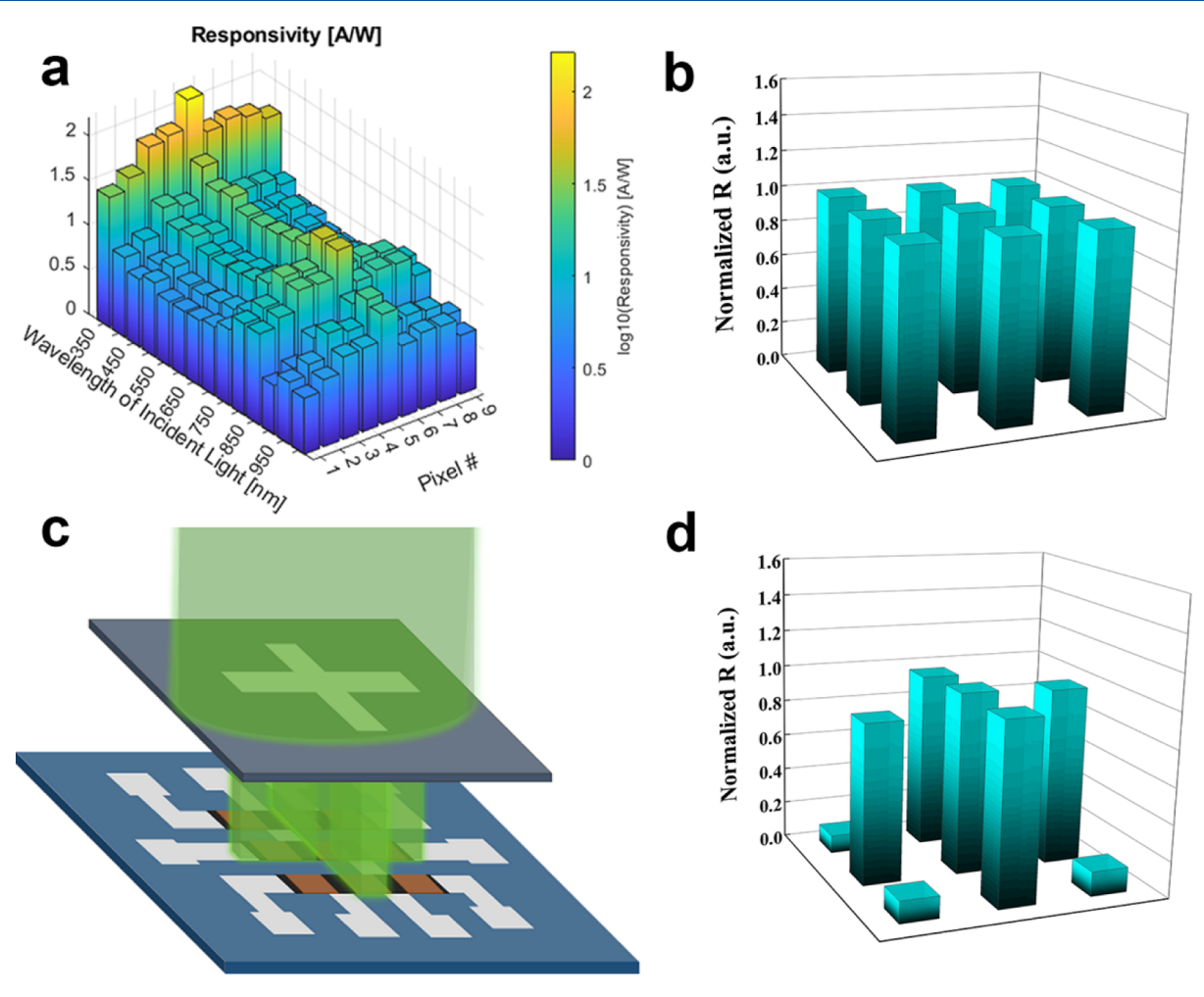


Figure 4. (a) Responsivity of the nine-channel PbS QD/graphene sensor array on the Si substrate vs wavelength and channel (pixel) for an incident light power of \sim 2.5 μ W and a bias voltage of 1 V. (b) Normalized responsivity of nine pixels at a wavelength of 500 nm. (c) Diagram of transmission imaging using a shadow mask with an "X" showing five center channels illuminated and four corner ones in the dark. (d) Normalized response of nine pixels using the normalization in (b), showing the results of imaging the "X" shadow mask.

spectrum at the chopper frequency used to measure the photocurrent. Figure 3d shows the corresponding D^* for the PbS QD/graphene photodetector as a function of the wavelength at an incident light power of 900 pW, and a bias voltage of 1.0 V. D^* is shown to decrease monotonically with increasing wavelength from 8.8×10^{11} Jones $\pm 0.19 \times 10^{11}$ Jones at 400 nm to 3.0×10^{11} Jones $\pm 0.07 \times 10^{11}$ Jones at 1000 nm. This trend is associated with the similar trend of R^* as a function of the wavelength as discussed above. If the chopper was operated at 55 Hz instead of 0.033 Hz, these D^* values would change very little owing to a factor of \sim 40 decrease in the noise at 55 Hz. Figure 3d exhibits the bias voltage dependence of R^* , the linear trend is expected from the graphene channel in PbS QD/graphene sensors. ¹⁰

Figure 4a illustrates the R^* measured on all nine pixels in the nine-channel PbS QD/graphene sensor array on Si in the wavelength range of 400–1000 nm. All nine channels show similar trends of wavelength dependence, while the nonuniformity of the R^* values is primarily associated with the nonuniformity of QD coating including thickness and distribution. In addition, other factors such as graphene quality and PbS QD/graphene interface may affect R^* uniformity from pixel to pixel, which may contribute to the moderate R^* nonuniformity shown in Figure 4a. This means a control of the

graphene growth and transfer; QD deposition and QD/ graphene interface engineering are important to achieving better R^* uniformity from pixel to pixel. At 400 nm, the R^* varies from 7.8-37.4 A/W from pixel to pixel, while a similar variation range of 6.7-28.0 and 4.3-17.1 A/W can be seen at 500 and 1000 nm, respectively. However, uniform normalized R* (Figure 4b) can be obtained by normalizing the measured response to R* value at 500 nm, at an optical power of 1112 nW, for each pixel in the algorithm developed for the Arduino ROIC. This allows a "machine-learning" treatment of the images taken with a PbS QD/graphene sensor array with moderate R* nonuniformity for better quality images. The imaging functionality of the nine-channel PbS QD/graphene sensor array was examined by recognizing the optical pattern of an "X" (Figure 4c) projected onto the array using the 500 nm illumination. The Arduino ROIC was used to automatically collect signal from all nine pixels, convert signal from analog to digital, and transfer that data to the computer. More details can be found in the Experimental Section and Supporting Information (Figure S3). Figure 4d shows the imaging result of the "X" collected on the nine-channel PbS QD/graphene sensor array. With normalization, fairly uniform R^* values were recorded on the five center pixels as expected. In contrast, the four corner pixels recorded negligible R* values. A video

showing imaging of the "X" pattern using the nine-channel PbS QD/graphene sensor array is included in the Supporting Information.

In order to image more complicated patterns, a scanning stage was adopted such that the projected pattern can be scanned across the array, thus a single pixel can be used to obtain a higher-resolution image than the nine pixels without scanning. The scanning system operates by moving the image, a shadow mask, horizontally across the array. Transmission of light through the shadow mask projects the image on the array which appears to move as viewed by the array when the mask is scanned back and forth. Once the horizontal scan is complete, the mask is moved slightly in the vertical direction and another horizontal scan is taken. This procedure is repeated until the desired number of vertical steps, with a chosen step size, has been reached. The obtained image can be improved slightly by imaging with all nine devices and taking the average (taking into account differences in each device's location in the array). Figure 5a shows the setup of the

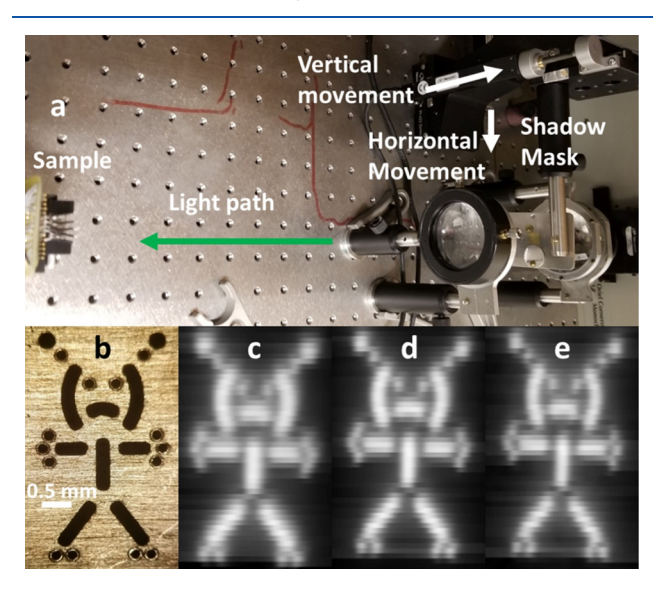


Figure 5. (a) Image scanning system showing the shadow mask location which is scanned horizontally and vertically via linear actuators to obtain a transmission image on the nine-channel PbS QD/graphene sensor array mounted at the "Sample" location. (b) Optical image of the shadow mask that is scanned through the light beam to create a transmission image on the array. (c–e) Images obtained by a nine-channel PbS QD/graphene sensor array on the Si substrate at wavelengths of (c) 400, (d) 500, and (e) 1000 nm.

scanning system. Using this system, images of a shadow mask (Figure 5b) with a minimum feature dimension of $\sim 200~\mu m$ have been taken at 400 nm (Figure 5c), 500 nm (Figure 5d), and 1000 nm (Figure 5e). While a higher resolution can be obtained at smaller wavelengths, the overall image quality at all three wavelengths is fairly good. Specifically, the minimum feature size of $\sim\!200~\mu m$, such as the eyes of the spaceman in the images, can be clearly seen. It should be noted that the image quality can be further improved when the optical setup is optimized.

The flexibility and transferability of QD/graphene nanohybrid sensor arrays are extraordinary properties that conventional rigid image sensors do not possess, making them possible to be integrated into flexible devices such as wearable devices. To demonstrate this feasibility, Figure 6a shows a

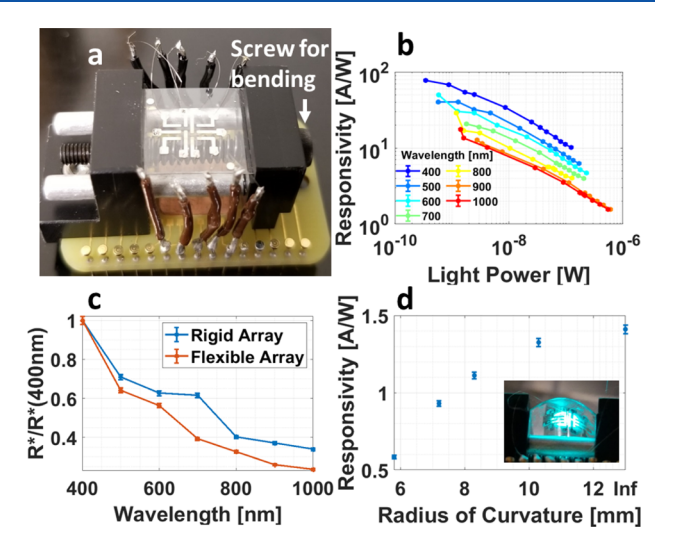


Figure 6. (a) Nine-channel PbS QD/graphene sensor array on the PET substrate and mounted on a bending vise. The screw indicated in the figure is turned to bring the two sides of the vise together to generate bending. (b) Normalized responsivity of the PET array vs incident light power for a few selected wavelengths and a bias voltage of 1 V. (c) Responsivity of the flexible PET array as a function of incident light wavelength as well as the rigid Si array, both normalized at 400 nm for comparison. Incident light power was around 120 nW for this case with a bias voltage of 1 V. (d) Responsivity vs radius of curvature for the PET array with 500 nm illumination. The light power for this case was 2.5 μ W, and the bias voltage was 1 V. The inset shows the array under bending conditions and illuminated by 500 nm light.

nine-channel PbS QD/graphene sensor array fabricated on a PET substrate. Since this is the first report of a flexible focal plane array based on QD/graphene photodetectors, to our knowledge, we aim to answer two important questions: (1) how great is the performance difference between nine-channel PbS QD/graphene sensor arrays on flexible PET substrates as compared to their counterparts on rigid Si substrates under the same device fabrication condition? and (2) what is the impact of bending-induced strain on the performance of the ninechannel PbS QD/graphene sensor arrays on flexible PET? Figure 6b shows the R* versus incident light power measured in the 400-1000 nm wavelength range on the nine-channel PbS QD/graphene sensor array on flexible PET. As compared to the similar measurement on the nine-channel PbS QD/ graphene sensor arrays on the rigid Si substrate (Figure 3c), the R* shows a similar dependence on the light power qualitatively, despite overall lower values in the devices on PET. Keep in mind the nine-channel PbS QD/graphene sensor arrays on the rigid Si substrate or flexible PET were made using the same conditions. Therefore, this difference could be attributed to the smaller PbS QD thickness, 50-70 nm, in the devices on PET since the rougher surface of PET affects spread of the PbS QD suspension, resulting in significantly smaller QD layer thickness. This can be seen quantitatively in Figure S4, which shows the optimal thickness for responsivity is around 250-300 nm. This argument is supported by the approximately similar wavelength dependence of the normalized R^*/R^* (400 nm) in Figure 6c. Interestingly, the dynamic range of the R* linearity in the PbS QD/Gr photodetectors on flexible substrates is similar to that of their counterparts on rigid substrates.

A series of bending conditions of the nine-channel PbS QD/ graphene sensor array on flexible PET to different radius of curvatures were conducted, followed by R* measurement, to examine the impact of strain from bending on the performance of the flexible imager. It should be noted that bending would result in different PbS QD/graphene sensors on the flexible nine-channel array to have different distances to the light source during the measurement. However, the light intensity attenuation in an ambient environment over a distance of 5 mm is ≪1% for a wavelength of 650 nm.³⁷ Furthermore, the light beam used in this experiment was collimated; the loss of light due to dispersion is also negligible. Therefore, the effect of the bending on the light intensity variation across the ninechannel array is unlikely significant. Figure 6d shows the R^* as a function of the radius of curvature, while the inset exhibits the array under the bending. At a large radius of curvature down to ~ 10.3 mm, no degradation of the R^* was observed. With further reduction of the radius of curvature, a monotonically decreasing R^* is shown. It should be noted that when the bending was released, the R* returned to its original value, indicating the pixels were intact during the bending in the range shown in Figure 6d. In addition, it should be mentioned that the flexible PbS QD/Gr sensors on PET exhibited excellent stability of performance with respect to the bending test exceeding 50 bending cycles within the range of radius of curvature shown in Figure 6d.

Figure 7a-c demonstrates the images taken using the ninechannel PbS QD/graphene sensor array on flexible PET at

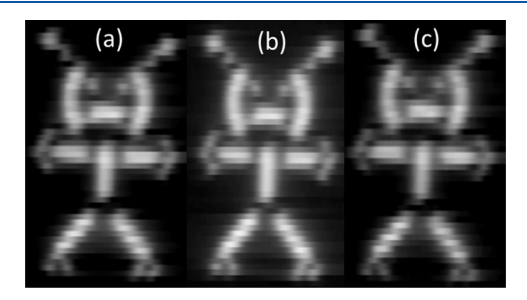


Figure 7. Images taken with a nine-channel PbS QD/graphene nanohybrid sensor array on PET at wavelengths of (a) 400, (b) 500, and (c) 1000 nm, respectively.

400, 500, and 1000 nm wavelengths. Again, a comparable imaging quality is demonstrated at the broadband spectrum of 400–1000 nm. In particular, the 200 μ m minimum features, such as the eyes of the spaceman, have been shown on all three images. Figure 8 compares the spaceman images taken by the nine-channel PbS QD/graphene sensor array on flexible PET, while the array was held flat (Figure 8a) and bent at a radius of curvature of 5.0 mm (Figure 8b). The comparable image quality between them illustrates the feasibility of the flexible PbS QD/graphene sensor arrays operating on curved surfaces.

4. CONCLUSIONS

In summary, this work explores fabrication, characterization, and integration of flexible PbS QD/graphene nanohybrid photodetector arrays with a low-cost Arduino ROIC for imaging. A nine-channel PbS QD/graphene array has been demonstrated as a prototype on which several key steps have been developed including the following: (1) fabrication of graphene channels using photolithography, (2) deposition of PbS QDs on the graphene channel, followed with ligand

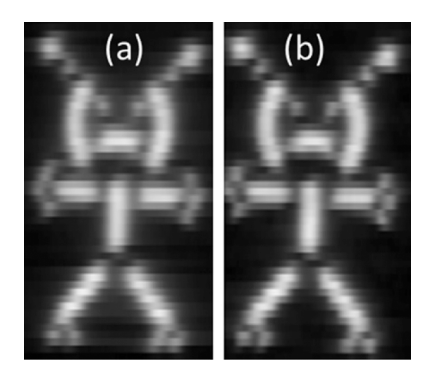


Figure 8. Images taken with a nine-channel PbS QD/graphene nanohybrid sensor array on PET with the array (a) flat and (b) bent at a radius of curvature of 5 cm.

exchange for passivation of the PbS QD surface states as well as establishment of a charge-transfer pathway from QD to graphene, (3) a testing structure for arrays fabricated on flexible or rigid substrates, and 4) signal acquisition from the nine pixels and image processing for display on a computer via the Arduino ROIC. On the nine-channel PbS QD/graphene imaging array, high uniformity has been demonstrated in photoresponse in the broadband spectrum from UV to NIR with pixel performance comparable to the best on the individual PbS QD/graphene devices. In addition, a flexible version was fabricated and shown to have consistent response down to a radius of curvature of 10.3 mm. Last, imaging at variable wavelengths and light intensity has been demonstrated at the speed currently limited by the response speed of the PbS QD/graphene individual pixels, which can be improved with optimization of the pixel. Therefore, this result provides a lowcost, facile scheme for the development of flexible QD/ graphene sensor arrays.

ASSOCIATED CONTENT

Supporting Information

The Supporting Information is available free of charge at https://pubs.acs.org/doi/10.1021/acsanm.2c03839.

Noise spectra of nine pixels; dynamic response with the light chopped at a frequency of 55 Hz; block diagram illustrating how data is collected using the Arduino Due; responsivity versus number of spin coat cycles; and responsivity versus light power versus pixel number (PDF)

Video generated by the nine-pixel array and Arduino ROIC showing a cross moving across the array in vertical and horizontal directions (MP4)

AUTHOR INFORMATION

Corresponding Authors

Andrew Shultz — Department of Physics and Astronomy, The University of Kansas, Lawrence, Kansas 66045, United States; Email: andjshultz@ku.edu

Bo Liu – Department of Physics and Astronomy, The University of Kansas, Lawrence, Kansas 66045, United States; orcid.org/0000-0003-0298-8238; Email: liubo@ku.edu

Judy Z. Wu – Department of Physics and Astronomy, The University of Kansas, Lawrence, Kansas 66045, United States; Email: jwu@ku.edu

Authors

Maogang Gong — Department of Physics and Astronomy, The University of Kansas, Lawrence, Kansas 66045, United States; Occid.org/0000-0002-2031-781X

Mohammed Alamri — Department of Physics and Astronomy, The University of Kansas, Lawrence, Kansas 66045, United States; Department of Physics, University of Umm Al-Qura, Makkah 21955, Saudi Arabia; orcid.org/0000-0002-7473-8644

Michael Walsh — Department of Energy's National Security Campus, Kansas City, Missouri 64147, United States Russell C. Schmitz — U.S. Army DEVCOM CSISR Center, Research & Technology Integration Directorate, Ft. Belvoir, Virginia 22060, United States

Complete contact information is available at: https://pubs.acs.org/10.1021/acsanm.2c03839

Author Contributions

¹A.S. and B.L. contributed equally to this work.

Notes

The authors declare no competing financial interest.

ACKNOWLEDGMENTS

The authors thank the support by Honeywell Federal Manufacturing & Technologies, LLC under contract no. DE-NA-0002839 with the U.S. Department of Energy/National Nuclear Security Administration. The United States Government retains and the publisher, by accepting the article for publication, acknowledges that the United States Government retains a nonexclusive, paid-up, irrevocable, world-wide license to publish or reproduce the published form of this manuscript, or allow others to do so, for United States Government purposes. This research was also supported in part by US Army grant W909MY-21-C-0033 and National Science Foundation grants NSF-ECCS-1809283 and NSF-DMR-1909292.

■ REFERENCES

- (1) Konstantatos, G.; Badioli, M.; Gaudreau, L.; Osmond, J.; Bernechea, M.; de Arquer, F. P. G.; Gatti, F.; Koppens, F. H. L. Hybrid Graphene-Quantum Dot Phototransistors with Ultrahigh Gain. *Nat. Nanotechnol.* **2012**, *7*, 363–368.
- (2) Tang, J.; Kemp, K. W.; Hoogland, S.; Jeong, K. S.; Liu, H.; Levina, L.; Furukawa, M.; Wang, X.; Debnath, R.; Cha, D.; Chou, K. W.; Fischer, A.; Amassian, A.; Asbury, J. B.; Sargent, E. H. Colloidal-Quantum-Dot Photovoltaics Using Atomic-Ligand Passivation. *Nat. Mater.* **2011**, *10*, 765–771.
- (3) Ip, A. H.; Thon, S. M.; Hoogland, S.; Voznyy, O.; Zhitomirsky, D.; Debnath, R.; Levina, L.; Rollny, L. R.; Carey, G. H.; Fischer, A.; Kemp, K. W.; Kramer, I. J.; Ning, Z.; Labelle, A. J.; Chou, K. W.; Amassian, A.; Sargent, E. H. Hybrid Passivated Colloidal Quantum Dot Solids. *Nat. Nanotechnol.* **2012**, *7*, 577–582.
- (4) Lu, H.; Carroll, G. M.; Neale, N. R.; Beard, M. C. Infrared Quantum Dots: Progress, Challenges, and Opportunities. *ACS Nano* **2019**, *13*, 939–953.
- (5) Dean, C. R.; Young, A. F.; Meric, I.; Lee, C.; Wang, L.; Sorgenfrei, S.; Watanabe, K.; Taniguchi, T.; Kim, P.; Shepard, K. L.; Hone, J. Boron Nitride Substrates for High-Quality Graphene Electronics. *Nat. Nanotechnol.* **2010**, *5*, 722–726.
- (6) Chen, J. H.; Jang, C.; Xiao, S. D.; Ishigami, M.; Fuhrer, M. S. Intrinsic and extrinsic performance limits of graphene devices on SiO2. *Nat. Nanotechnol.* **2008**, *3*, 206–209.
- (7) Geim, A. K.; Novoselov, K. S. The Rise of Graphene. *Nat. Mater.* **2007**, *6*, 183–191.
- (8) Geim, A. K. Graphene: Status and Prospects. Science 2009, 324, 1530–1534.

- (9) Wu, J.; Ma, H.; Yin, P.; Ge, Y.; Zhang, Y.; Li, L.; Zhang, H.; Lin, H. Two-Dimensional Materials for Integrated Photonics: Recent Advances and Future Challenges. *Small Sci.* **2021**, *1*, 2000053.
- (10) Wu, J.; Gong, M.; Schmitz, R. C.; Liu, B., Quantum Dot/Graphene Heterostructure Nanohybrid Photodetectors. In *Quantum Dot Photodetectors*, Springer, Cham: 2021; Vol. 30, pp 215–248.
- (11) Kwak, D.-H.; Lim, D.-H.; Ra, H.-S.; Ramasamy, P.; Lee, J.-S. High performance hybrid graphene-CsPbBr3—xIx perovskite nanocrystal photodetector. *RSC Adv.* **2016**, *6*, 65252–65256.
- (12) Gong, M.; Liu, Q.; Cook, B.; Kattel, B.; Wang, T.; Chan, W. L.; Ewing, D.; Casper, M.; Stramel, A.; Wu, J. Z. All-Printable ZnO Quantum Dots/Graphene Van Der Waals Heterostructures for Ultrasensitive Detection of Ultraviolet Light. ACS Nano 2017, 11, 4114–4123.
- (13) Yang, C.; Feng, S.; Tang, L.; Shen, J.; Wei, X.; Shi, H. Electrochemical Epitaxial Grown PbS Nanorods Array on Graphene Film for High-Performance Photodetector. *Adv. Mater. Interfaces* **2021**, *8*, 2001464.
- (14) Jiang, H.; Wang, M.; Fu, J.; Li, Z.; Shaikh, M. S.; Li, Y.; Nie, C.; Sun, F.; Tang, L.; Yang, J.; Qin, T.; Zhou, D.; Shen, J.; Sun, J.; Feng, S.; Zhu, M.; Kentsch, U.; Zhou, S.; Shi, H.; Wei, X. Ultrahigh Photogain Short-Wave Infrared Detectors Enabled by Integrating Graphene and Hyperdoped Silicon. ACS Nano 2022, 16, 12777—12785.
- (15) Jiang, H.; Wei, J.; Sun, F.; Nie, C.; Fu, J.; Shi, H.; Sun, J.; Wei, X.; Qiu, C.-W. Enhanced Photogating Effect in Graphene Photodetectors Via Potential Fluctuation Engineering. ACS Nano 2022, 16, 4458–4466.
- (16) Goossens, S.; Navickaite, G.; Monasterio, C.; Gupta, S.; Piqueras, J. J.; Pérez, R.; Burwell, G.; Nikitskiy, I.; Lasanta, T.; Galán, T.; Puma, E.; Centeno, A.; Pesquera, A.; Zurutuza, A.; Konstantatos, G.; Koppens, F. Broadband image sensor array based on graphene-CMOS integration. *Nat. Photonics* **2017**, *11*, 366–371.
- (17) Guenter, B.; Joshi, N.; Stoakley, R.; Keefe, A.; Geary, K.; Freeman, R.; Hundley, J.; Patterson, P.; Hammon, D.; Herrera, G.; Sherman, E.; Nowak, A.; Schubert, R.; Brewer, P.; Yang, L.; Mott, R.; McKnight, G. Highly Curved Image Sensors: A Practical Approach for Improved Optical Performance. *Opt. Express* **2017**, *25*, 13010–13023.
- (18) Yan, Y.; Wu, X.; Chen, Q.; Liu, Y.; Chen, H.; Guo, T. High-Performance Low-Voltage Flexible Photodetector Arrays Based on All-Solid-State Organic Electrochemical Transistors for Photosensing and Imaging. ACS Appl. Mater. Interfaces 2019, 11, 20214—20224.
- (19) Li, L.; Gu, L.; Lou, Z.; Fan, Z.; Shen, G. ZnO Quantum Dot Decorated Zn2SnO4 Nanowire Heterojunction Photodetectors with Drastic Performance Enhancement and Flexible Ultraviolet Image Sensors. ACS Nano 2017, 11, 4067–4076.
- (20) Gong, M.; Sakidja, R.; Goul, R.; Ewing, D.; Casper, M.; Stramel, A.; Elliot, A.; Wu, J. Z. High-Performance All-Inorganic CsPbCl3 Perovskite Nanocrystal Photodetectors with Superior Stability. ACS Nano 2019, 13, 1772–1783.
- (21) Choi, C.; Choi, M. K.; Liu, S.; Kim, M. S.; Park, O. K.; Im, C.; Kim, J.; Qin, X.; Lee, G. J.; Cho, K. W.; Kim, M.; Joh, E.; Lee, J.; Son, D.; Kwon, S. H.; Jeon, N. L.; Song, Y. M.; Lu, N.; Kim, D. H. Human eye-inspired soft optoelectronic device using high-density MoS2-graphene curved image sensor array. *Nat. Commun.* 2017, *8*, 1664.
- (22) Polat, E. O.; Mercier, G.; Nikitskiy, I.; Puma, E.; Galan, T.; Gupta, S.; Montagut, M.; Piqueras, J. J.; Bouwens, M.; Durduran, T.; Konstantatos, G.; Goossens, S.; Koppens, F. Flexible Graphene Photodetectors for Wearable Fitness Monitoring. *Sci. Adv.* **2019**, *5*, No. eaaw7846.
- (23) Kim, J.; Kwon, S. M.; Kang, Y. K.; Kim, Y. H.; Lee, M. J.; Han, K.; Facchetti, A.; Kim, M. G.; Park, S. K. A Skin-Like Two-Dimensionally Pixelized Full-Color Quantum Dot Photodetector. *Sci. Adv.* **2019**, *5*, No. eaax8801.
- (24) Xia, K.; Wu, W.; Zhu, M.; Shen, X.; Yin, Z.; Wang, H.; Li, S.; Zhang, M.; Wang, H.; Lu, H.; Pan, A.; Pan, C.; Zhang, Y. CVD Growth of Perovskite/Graphene Films for High-Performance Flexible Image Sensor. *Sci. Bull.* **2020**, *65*, 343–349.

- (25) Kim, Y.-J.; Saviers, K. R.; Fisher, T. S.; Irazoqui, P. P. Continuous Glucose Monitoring with a Flexible Biosensor and Wireless Data Acquisition System. *Sens. Actuators, B* **2018**, 275, 237–243.
- (26) Cook, B.; Liu, Q.; Liu, J.; Gong, M.; Ewing, D.; Casper, M.; Stramel, A.; Wu, J. Facile Zinc Oxide Nanowire Growth on Graphene Via a Hydrothermal Floating Method: Towards Debye Length Radius Nanowires for Ultraviolet Photodetection. *J. Mater. Chem. C* **2017**, *5*, 10087–10093.
- (27) Liu, Q.; Gong, Y.; Wilt, J. S.; Sakidja, R.; Wu, J. Synchronous Growth of AB-Stacked Bilayer Graphene on Cu by Simply Controlling Hydrogen Pressure in CVD Process. *Carbon* **2015**, 93, 199–206
- (28) Xu, G.; Lu, R.; Liu, J.; Chiu, H.-Y.; Hui, R.; Wu, J. Z. Photodetection Based on Ionic Liquid Gated Plasmonic Ag Nanoparticle/Graphene Nanohybrid Field Effect Transistors. *Adv. Opt. Mater.* **2014**, *2*, 729–736.
- (29) Gong, M.; Alamri, M.; Ewing, D.; Sadeghi, S. M.; Wu, J. Z. Localized Surface Plasmon Resonance Enhanced Light Absorption in AuCu/CsPbCl3 Core/Shell Nanocrystals. *Adv. Mater.* **2020**, 32, No. e2002163.
- (30) Cook, B.; Gong, M.; Ewing, D.; Casper, M.; Stramel, A.; Elliot, A.; Wu, J. Inkjet Printing Multicolor Pixelated Quantum Dots on Graphene for Broadband Photodetection. *ACS Appl. Nano Mater.* **2019**, *2*, 3246–3252.
- (31) Gong, M.; Liu, Q.; Goul, R.; Ewing, D.; Casper, M.; Stramel, A.; Elliot, A.; Wu, J. Z. Printable Nanocomposite FeS2-PbS Nanocrystals/Graphene Heterojunction Photodetectors for Broadband Photodetection. ACS Appl. Mater. Interfaces 2017, 9, 27801–27808
- (32) Gong, M.; Sakidja, R.; Liu, Q.; Goul, R.; Ewing, D.; Casper, M.; Stramel, A.; Elliot, A.; Wu, J. Z. Broadband Photodetectors Enabled by Localized Surface Plasmonic Resonance in Doped Iron Pyrite Nanocrystals. *Adv. Opt. Mater.* **2018**, *6*, 1701241.
- (33) Ma, C.; Gong, Y.; Lu, R.; Brown, E.; Ma, B.; Li, J.; Wu, J. Detangling Extrinsic and Intrinsic Hysteresis for Detecting Dynamic Switch of Electric Dipoles Using Graphene Field-Effect Transistors on Ferroelectric Gates. *Nanoscale* **2015**, *7*, 18489–18497.
- (34) Lu, R.; Liu, J.; Luo, H.; Chikan, V.; Wu, J. Z. Graphene/Gase-Nanosheet Hybrid: Towards High Gain and Fast Photoresponse. *Sci. Rep.* **2016**, *6*, 19161.
- (35) Liu, B.; Gutha, R. R.; Kattel, B.; Alamri, M.; Gong, M.; Sadeghi, S. M.; Chan, W. L.; Wu, J. Z. Using Silver Nanoparticles-Embedded Silica Metafilms as Substrates to Enhance the Performance of Perovskite Photodetectors. ACS Appl. Mater. Interfaces 2019, 11, 32301–32309.
- (36) Li, A.; Chen, Q.; Wang, P.; Gan, Y.; Qi, T.; Wang, P.; Tang, F.; Wu, J. Z.; Chen, R.; Zhang, L.; Gong, Y. Ultrahigh-Sensitive Broadband Photodetectors Based on Dielectric Shielded MoTe₂/Graphene/SnS₂ P-G-N Junctions. *Adv. Mater.* **2019**, *31*, 1805656.
- (37) Abd Ali, M. A.; Mohammed, M. A. Effect of Atmospheric Attenuation on Laser Communications for Visible and Infrared Wavelengths. *J. Al-Nahrain Univ. Sci.* **2013**, *16*, 133–140.

□ Recommended by ACS

Remarkable Noise Reduction in High-Stability Self-Powered Doped Graphene/Si-Quantum Dot Broadband Photodetectors by Using Graphene Quantum Dots as an I...

Chan Wook Jang, Suk-Ho Choi, et al.

JULY 21, 2022

ACS SUSTAINABLE CHEMISTRY & ENGINEERING

READ 🗹

Dirac Point Modulated Self-Powered Ultrasensitive Photoresponse and Color-Tunable Electroluminescence from Flexible Graphene/Metal-Organic Frameworks/Graphen...

Krishna Prasad Bera, Yang-Fang Chen, et al.

MAY 11, 2022

ACS APPLIED ELECTRONIC MATERIALS

READ 🗹

Wide Bandgap Tuning of Violet Phosphorus Quantum Dots by Functionalization

Rongzheng Zhao, Jinying Zhang, et al.

AUGUST 26, 2022

THE JOURNAL OF PHYSICAL CHEMISTRY LETTERS

READ 🗹

Graphene-Coated Substrate-Mediated Photoresponse from MoS,/UCNP Nanohybrid-Based Photodetectors

Digvijay Singh Tomar, Surojit Chattopadhyay, et al.

NOVEMBER 10, 2022

ACS APPLIED ELECTRONIC MATERIALS

READ 🗹

Get More Suggestions >